Nucleic Acids Research, 2025, **53**, gkaf351
https://doi.org/10.1093/nar/gkaf351
RNA and RNA-protein complexes

Mechanistic insights into the activity of SARS-CoV-2 RNA polymerase inhibitors using single-molecule FRET

Danielle Groves[1], Rory Cunnison[1], Andrew McMahon[1], Haitian Fan[2], Jane Sharps[2], Adrian Deng[3], Jeremy R. Keown[3], Ervin Fodor[2], Nicole C. Robb[1,*]

[1]Warwick Medical School, University of Warwick, Coventry, CV4 7AL, United Kingdom
[2]Sir William Dunn School of Pathology, University of Oxford, Oxford, OX1 3PU, United Kingdom
[3]School of Life Sciences, University of Warwick, Coventry, CV4 7AL, United Kingdom
[*]To whom correspondence should be addressed. Email: Nicole.Robb@warwick.ac.uk

Abstract

The COVID-19 pandemic, caused by the SARS-CoV-2 virus, has resulted in significant global mortality, with over 7 million cases reported. Despite extensive research and high vaccination rates, highly mutated forms of the virus continue to circulate. It is therefore important to understand the viral lifecycle and the precise molecular mechanisms underlying SARS-CoV-2 replication. To address this, we developed a single-molecule Förster resonance energy transfer (smFRET) assay to directly visualize and analyse *in vitro* RNA synthesis by the SARS-CoV-2 RNA-dependent RNA polymerase (RdRp). We purified the minimal replication complex, comprising nsp12, nsp7, and nsp8, and combined it with fluorescently labelled RNA substrates, enabling real-time monitoring of RNA primer elongation at the single-molecule level. This platform allowed us to investigate the mechanisms of action of key inhibitors of SARS-CoV-2 replication. In particular, our data provides evidence for remdesivir's mechanism of action, which involves polymerase stalling and subsequent chain termination dependent on the concentration of competing nucleotide triphosphates. Our study demonstrates the power of smFRET to provide dynamic insights into SARS-CoV-2 replication, offering a valuable tool for antiviral screening and mechanistic studies of viral RdRp activity.

Graphical abstract

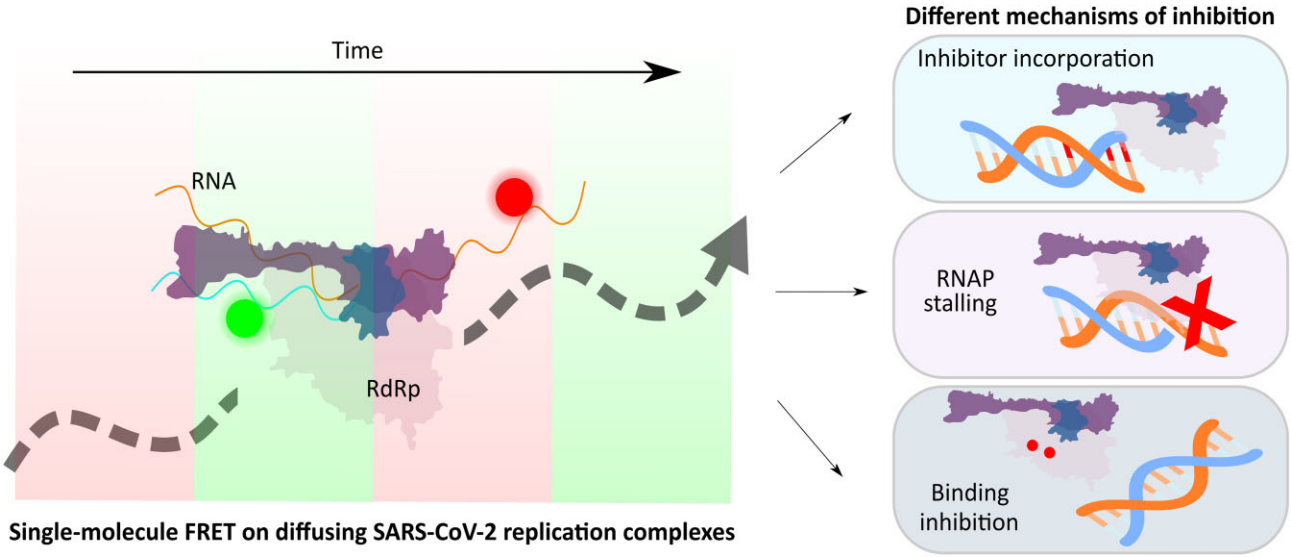

Introduction

Coronaviruses are positive-sense single-stranded RNA viruses of the order Nidovirales [1], which have significant epidemic and pandemic potential. This is evidenced by the seven known human circulating coronaviruses [2–5]. The emergence of the novel SARS-CoV-2 virus at the end of 2019 resulted in the COVID-19 pandemic that has infected millions of people and caused worldwide social and economic disruption. Therefore, understanding the exact molecular details of how coronaviruses replicate is important, particularly for the development of intervention strategies. To date, much of our knowledge of SARS-CoV-2 replication has relied on data obtained using ensemble methods that report on the mean properties of billions of molecules, averaging the measured parameters over the entire molecular population. Single-molecule techniques allow real-time studies of viral replication with the advantage

Received: October 17, 2024. **Revised:** April 8, 2025. **Editorial Decision:** April 12, 2025. **Accepted:** April 16, 2025

that they can provide direct observations of just one molecule at a time.

The SARS-CoV-2 virus contains a 30 kb single-stranded positive-sense genome that is replicated by the viral RNA-dependent RNA polymerase (RdRp) [6, 7] which also 'transcribes' sub-genomic length negative sense RNA templates to make sub-genomic messenger RNA which encode the viral structural and accessory proteins [6, 8]. The RdRp is unique to the virus, relatively conserved and essential for viral spread, making it an important target for potential treatments. Several cryo-EM studies of the SARS-CoV-2 RdRp alone [9–11] or bound to RNA [12] have elucidated the basic structure of the complex. The complex consists of three types of non-structural proteins (nsps): a single copy of nsp12, which contains the RdRp active site and the *Nidovirus* RdRp-associated nucleotidyltransferase domain which acts as a capping enzyme [13], a single copy of nsp7, suggested to be responsible for stabilization of regions of nsp12 thought to be involved in RNA binding [11], and two copies of nsp8, proposed to be essential for processivity of the polymerase [9, 10]. It is believed that nsp12, nsp7, and nsp8 represent a minimal replication transcription complex (the RTC) capable of replicating RNA, making the complex an attractive target for antiviral drug development [12].

Structures of the SARS-CoV-2 RdRp reveal a conserved structure for the RdRp which does not change significantly upon RNA binding [11, 14], unlike other RNA viruses such as the Influenza polymerase [15]. Cryo-electron microscopy (cryo-EM) and biochemical studies of the replicating RdRp [11, 12] show that during replication, the incoming nucleotide triphosphates (NTPs) enter the entry channel and are then stabilized in the active site of nsp12 by hydrogen-bonding, during which time the RdRp adopts the 'pre-translocation' state. The complex adopts a 'post-translocation' state when primer RNA enters the +1 position within the RNA-binding cleft. The polymerase domain of nsp12 contains aspartate residues D760 and D761, which bind to two Mg^{2+} ions before nucleotide addition [11, 12]. Watson–Crick base pairing between template and product RNA occurs during nucleotide incorporation, before the RdRp assumes the post-translocation conformation of RdRp. The nsp8 pair form positive charges either side of the active site with long helical 'sliding poles' which pull negatively charged RNA through the complex [10, 12].

Structural insights into the SARS-CoV-2 RdRp have allowed the function of a variety of non-nucleoside or nucleoside analogue inhibitors to be explored. For example, remdesivir is a broad-spectrum antiviral medicine that was originally developed to treat hepatitis C [16] and filoviruses such as Ebola [17] before being used as a post-infection treatment for COVID-19. Remdesivir is an adenosine analogue that acts as a competitive inhibitor of viral RdRps. The primary mechanism of inhibition has been suggested to be the incorporation of remdesivir triphosphate into nascent viral RNA by the viral RdRp, resulting in chain termination [18–20]. Unlike many other chain terminators, this is not mediated by preventing addition of the immediately subsequent nucleotide, but is instead delayed, occurring after additional bases have been added to the growing RNA chain. For MERS-CoV, SARS-CoV-1, and SARS-CoV-2, arrest of RNA synthesis occurs after incorporation of three additional nucleotides [19, 20]. Because of misincorporation of remdesivir, the analogue may be incorporated into the viral RNA template strand, which has also been shown to block RNA synthesis via a second, template-dependent inhibition mechanism [21]. Suramin is an example of a non-nucleoside inhibitor that has been shown to bind directly to the SARS-CoV-2 RdRp, and results in inhibition by blocking the binding of the RNA template strand and preventing entry of product RNA into the active site [22].

Here, we have used a solution-based single-molecule Förster resonance energy transfer (smFRET) assay to measure the dynamic conformational changes that occur during SARS-CoV-2 RdRp-mediated RNA extension and inhibition. We have shown that we can reconstitute minimal viral replication complexes *in vitro* and monitor the conformational changes that take place in RNA during RdRp-mediated extension via the movement of fluorescence dyes positioned on the RNA. We have applied this approach to probe the mechanisms of action of both a nucleoside and non-nucleoside inhibitor of SARS-CoV-2, validating their inhibition and differentiating between different mechanisms of action. This technique is therefore well suited to deciphering the mechanisms involved in viral replication inhibition, and we anticipate can be further applied to the screening of multiple other viral polymerases and inhibitors.

Materials and methods

RNA

We ordered minimal RNA oligonucleotides from Integrated DNA Technologies (IDT) based on the sequences in a cryo-EM structure of SARS-CoV-2 RdRp [23], conjugated to fluorescent labels Cy3, Cy5, or ATTO647 via six-carbon linkers. The sequences and positions of the fluorescent dyes are described in the figures and in Supplementary Table S1. Template and primer RNAs were annealed at a final concentration of 300 nM in hybridization buffer [20 mM Tris-HCl pH 8.0, 1 mM ethylenediaminetetraacetic acid (EDTA), 500 mM NaCl] using a single cycle temperature gradient from 95°C to 4°C. The thermocycler was set to cycle through 95°C, 90°C, and 85°C for 1 min each, followed by 75°C for 2 min, 65°C for 5 min, 45°C for 10 min, 25°C for 5 min, and hold at 4°C.

Protein

The expression and purification of nsps has been published previously [13, 24]. Briefly, the SARS-CoV-2 RdRp wild-type (WT) nsp12 and active site mutant nsp12 D760A/D761A were cloned into a MultiBac baculovirus with the pFL transfer vector [25] with a histidine tag along with a Tobacco Etch Virus (TEV) protease cleavable protein-A tag at the C-terminus (nsp12-His10-TEV-prot.A construct). The baculoviruses for overexpressing nsp12 and nsp12 D760A/D761A were generated by following the protocol by Berger *et al.* (2008) [25]. For overexpression, Sf9 cells were infected with recombinant baculovirus at a multiplicity of infection of 1 for 3 days before harvesting. One to two litres of sf9 pellet(s) was resuspended in wash buffer [50 mM HEPES-NaOH, pH 7.5, 300 mM NaCl, 10% glycerol, 0.05% n-Octyl β-d-thioglucopyranoside (OTG), 1 mM dithiothreitol (DTT)] with protease inhibitor before cell lysis by sonication. The cell lysate was centrifuged at 35 000 × *g* for 45 min at 4°C and the supernatant was incubated with 1 ml IgG sepharose per litre of cell culture for 3–4 h at 4°C. The solution was washed three times with wash buffer, then the protein A tag was cleaved with TEV protease (0.5–1 mg TEV/l cell culture, in the presence of 1 mM DTT), overnight at 4°C. The next day,

the supernatant (protein A tag-cleaved protein) was concentrated to 0.5–2 ml and loaded on to a Superdex 200 10/300 increase column in size exclusion chromatographic (SEC) running buffer [25 mM HEPES-Na (pH 7.5), 100 mM NaCl, 2 mM $MgCl_2$, 1 mM DTT].

SARS-CoV-2 nsp7 and nsp8 were inserted into plasmids containing a lac promoter, 3C protease-cleavable GST tag (GST-3C-nsp7 and GST-3C-nsp8) and ampicillin resistance gene, which were used to transform BL21 *Escherichia coli*. Cells were induced with 0.5 mM Isopropyl β-D-1- thiogalactopyranoside when OD600 = 0.6–0.8, then the cell culture was grown at 18°C overnight before harvesting by centrifugation at 3500 × *g* for 15 min at 4°C. One to two liters of *E. coli* pellet(s) was resuspended in wash buffer (50 mM HEPES-NaOH, pH 7.5, 300 mM NaCl, 10% glycerol, 0.05% OTG, 1 mM DTT) with protease inhibitor before cell lysis by sonication. The cell lysate was spun down and the supernatant was incubated with 1 ml GST Sepharose per litre of cell culture for 3–4 h at 4°C. The solution was washed three times with wash buffer, then the GST tag was cleaved with 3C protease (0.2–0.5 mg homemade 3C/l cell culture, in the presence of 1 mM DTT), overnight at 4°C. The next day, the supernatant (tag-cleaved protein) was concentrated to 0.5–2 ml and loaded on to a Superdex 75 10/300 increase column in the same SEC running buffer.

SEC fractions were checked by sodium dodecyl sulfate–polyacrylamide gel electrophoresis (SDS–PAGE) against the pre-stained precision plus 10–250 kDa Bio-Rad ladder (161–0373) and those with target protein were collected and concentrated to ∼5–10 mg/ml with an Amicon Millipore MWCO tube (100 kD cutoff for nsp12 and 10 kD for nsp7/nsp8), aliquoted and flash-frozen in liquid nitrogen before storage at −80°C. The final products were also checked by SDS–PAGE.

In vitro activity assays

Final concentrations of 500 nM RdRp were incubated with 50 nM pre-annealed RNA for 10 min at 30°C in a 3 μl reaction containing master mix (MM) (5 mM $MgCl_2$, 0.5 mM NTPs, 10 mM KCl, 1 U/μl RNasin, 0.1 mM DTT) and protein storage buffer (PSB) (6.25 mM HEPES, 37.5 mM NaCl, 0.5 mM $MgCl_2$, 0.25 mM DTT, 20% glycerol). A low NTP concentration refers to 100 fold lower NTPs, which is a final concentration of 5 μM.

For remdesivir and suramin, compounds were resuspended in water before being diluted to the final concentrations stated in the figures in PSB, replacing PSB during incubation with protein–RNA complexes. For denaturing gels, samples were denatured by incubation with loading dye (80% formamide, 10 mM EDTA) at 95°C for 3 min before being loaded onto a 6 M urea, 20% polyacrylamide denaturing gel [dimensions 16.5 × 22 cm (w x h), C.B.S. Scientific] and run at 450 V for 2.5 h. For native gels, this step was replaced by adding a loading solution of 50% glycerol 1:1 with protein–RNA complexes and use of 4%–15% Bio-Rad Mini-PROTEAN TGX gels which can be run in sodium dodecyl sulphate-free tris-glycine running buffer. Gels were visualized using a Bio-Rad Chemidoc imaging system in the Cy3 and Cy5 emission ranges. In order to quantify how much of the RNA was extended, we took mean intensity measurements of each band per column using ImageJ in both channels, including a background fluorescence measurement for each column which was subtracted from the mean intensity to remove background fluorescence. The band was taken to represent RNA at a certain length based on comparison to the RNA control lanes. The relative ratio of unextended primer to extended primer was then determined by finding the intensity at the appropriate position and dividing by total intensity per column. The measurement was taken in the Cy5 channel if the Cy5-labelled primer was present, or in the Cy3 channel if the Cy3-labelled template or Cy3-labelled primer was present. Results were plotted using Graphpad Prism 10 and represent $n = 2$ or $n = 3$ gels.

FRET Positioning Software modelling

RNA was modelled using 3D models made on the RNA Composer 2 [26, 27] website and subsequently imported into Pymol and merged with the SARS-CoV-2 RdRp structure PDB 6YYT [12]. Fluorescence dyes are attached by a six-carbon linker to the selected nucleotides shown in the schematics for each experiment and are attached via the C5′ of the indicated sugar residue. We used FRET Positioning Software (FPS) [28] which models the accessible volume (AV) of each dye by considering the linker length, dye dimensions, and steric hindrance to produce an average dye position and dye clouds which can be plotted in Pymol to represent the available positions for each dye. The distance between the average dye positions was measured using the 'measure distance' function in Pymol and used to estimate the distance between dye pairs. Distance was converted into an estimated FRET efficiency using an R0 for the Cy3/Cy5 pair of 5.4 nm, as previously characterized [29–31].

Single-molecule fluorescence spectroscopy

The EI-FLEX confocal microscope (Exciting Instruments) was used for single-molecule FRET experiments using alternating-laser excitation (ALEX) to excite donor and acceptor fluorophores sequentially [32]. RdRp at a final concentration of 5 μM was incubated with fluorescently labelled RNA at a final concentration of 13.5 nM for 30 min at 30°C in MM and PSB before dilution to a final RNA concentration of ∼7 pM in confocal buffer ($MgCl_2$ 7 mM, KCl 10 mM, RNAsin 0.4 U/μl, DTT 0.2 mM, HEPES, pH 7.5 25 mM, NaCl 100 mM in water) for confocal imaging and analysis. We used a 2-laser line set up with 30–40 mW lasers at 520 and 638 nm. The 520 nm laser was used at 0.22 mW power with a 100 μs alternation period: OFF: 0 μs, ON: 45 μs, OFF: 55 μs, while the 638 nm laser power was 0.16 mW and alternating OFF: 50 μs, ON: 45 μs, OFF: 5 μs. The Exciting Instruments software was used to measure and evaluate the signals obtained [33].

Fluorescence correlation spectroscopy

The same microscope and experimental configuration as described above was used for fluorescence correlation spectroscopy (FCS) measurements; however RdRp–RNA complexes were diluted 1:1 with confocal buffer (∼7 nM) to reach a number of molecules between 1 and 10 (based on Count Rate/Brightness in kHz). Excitation was at 520 nm in continuous-wave fashion at 0.1 mW laser power. Photon-by-photon arrival times in the donor and acceptor channels were correlated using pulsed interleaved excitation analysis (PAM) with MATLAB [34]. Data in the manuscript were derived from autocorrelation in the green detection channel, where the confocal volume parameters were determined using rhodamine 6G and it's known diffusion coefficient 414 m^2/s [35].

The correlations over lag time were fitted using PAM and plotted in MATLAB.

Data analysis

The Exciting Instruments pipeline assigns fluorescent photons to donor or acceptor fluorophores based on photon arrival time and the two characteristic ratios, fluorophore stoichiometry, S, and apparent FRET efficiency, E.

Equation 1: Apparent FRET efficiency, E.

$$E = 1/(1 + (R/R0)^6 \quad (1)$$

where E is the FRET efficiency, R is the inter-fluorophore distance, and R0 is the Förster radius, a proportionality constant that depends on the interaction between the transition dipoles of donor and acceptor and represents the distance between the donor and the acceptor at which energy transfer is 50%.

Equation 2: Stoichiometry, S.

$$S = F_{D/D} + F_{A/D}/F_{D/D} + F_{A/D} + F_{A/A} \quad (2)$$

ALEX is used to alternately excite the donor (D) and acceptor (A) to determine the stoichiometry (S) of the molecules of interest taking into account signal (F) from the excited fluorophores. A two-dimensional histogram is plotted using S and E from fluorescent bursts above a certain threshold, and the one-dimensional E distribution of the populations within $0.4 < S < 0.8$. We fitted these distributions with Gaussian functions to identify a mean E value for each distribution using the EI cloud software and associated Jupyter notebooks: FRETBursts (version 0.7.1) [33]. The notebooks performed an all photon burst search and a dual channel burst search [36] to collect bursts above a threshold, where selected photons passed through the detector at a rate 6x higher than background. The 'FRET Analysis' notebook was modified to include the MultiFitter Gaussian model to fit 1 or more Gaussians, where the histogram and fit was displayed as a frequency (pdf = False) or probability density function (pdf = True) to determine the proportion of distinct populations, out of the total of fits. The 'Correction Factor Finder Alpha-Delta' and 'Correction Factor Finder Gamma-Beta' notebooks were used to find the correction factors α, δ, β, and γ.

Results

A minimal RTC is active *in vitro*

To establish a single-molecule SARS-CoV-2 RdRp replication assay we initially expressed and purified the minimal protein components needed for replication and transcription (the RTC): nsp12, nsp7, and nsp8, as well as a replication-deficient nsp12 mutant D760A/D761A (Fig. 1A). The nsp12-His10-TEV-prot.A constructs were expressed in sf9 insect cells while the GST-3C-nsp7 and GST-3C-nsp8 plasmid constructs were expressed in *E. coli* under a lac promoter, before being purified using size-exclusion chromatography. Gel electrophoresis of the purified proteins showed bands at the expected sizes: 110 kDa for nsp12 WT and nsp12 D760A/D761A, 22 kDa for nsp8 and 9.4 kDa for nsp7 (Fig. 1B); we note the presence of a small number of additional bands on the gel which are bacterial or insect cell proteins that co-purified with our target protein.

To demonstrate activity of the purified RTC, we adapted a previously described assay using ^{32}P- radiolabelled RNA to verify polymerase activity [13, 37] for use with fluorescently labelled RNA substrates. We preincubated the three nsps together to form a complex, before incubating with fluorescently labelled template and primer RNAs (Fig. 1C). Confirmation of activity is provided by extension of a short primer labelled with Cy5 from 20 to 30 nucleotides when RdRp is added (Fig. 1D). Using the assay, we were able to show that a Cy5-labelled primer strand was only extended when the polymerase was complexed with both primer and template RNA strands (Fig. 1E, lane 3). We have quantified this as a ratio of RNA extension from a 20 mer to 30 mer using the intensity of the extended band over the total intensity of all bands, showing that the majority of RNA is extended in this assay if polymerase and both strands of RNA are present (Fig. 1F). A Cy3-labelled primer was also extended in our assay, showing that *in vitro* activity is independent of the fluorescent dye (Fig. 1E, lane 12). As expected, the nsp12 active site mutant (D760A/D761A) demonstrated significantly lower activity than WT (Fig. 1E, lane 5); a small level of activity observed in some samples with D760A/D761A is likely due to purification of the mutant RdRp on the same column as WT protein. Overall, these results demonstrate that a purified minimal RTC was able to efficiently extend RNA labelled with fluorescent dyes.

A single-molecule extension assay detects conformational changes in RNA during replication

To measure RdRp-mediated replication using smFRET, we used a 43-nucleotide 'overhang' RNA template that was designed to form a self-annealed hairpin labelled with a Cy3 dye at the 5′ end (Fig. 2A). This template RNA was annealed to a shorter primer RNA, labelled with a Cy5 dye at position 12. Together, this template and primer RNA form a double-stranded construct that is predicted to bring the two dyes into close proximity, resulting in a high FRET signature. We hypothesized that upon RdRp and nucleotide addition the primer sequence would be extended, which in turn would open the self-annealed section of the template strand, resulting in the two dyes being separated and a decrease in the FRET signature (Fig. 2A). Our template design also ensures that extension will proceed in a nucleotide-dependent manner, with partial extension expected from addition of ATP only, whilst full extension will only be achieved when both ATP and uridine triphosphate (UTP) are added. To estimate the efficiency of energy transfer between the two fluorophores in our expected constructs we used FPS to calculate the AVs that the Cy3 and Cy5 dyes could occupy when bound to the RNA in each configuration. We then measured the distance between the AVs of the two dyes both for the RNA alone or RNA fully extended by the RdRp (Fig. 2B). This measured distance allowed us to estimate the FRET efficiency for each dye pair, providing us an estimated FRET efficiency, E, of ∼0.99 for the RNA only and of ∼0.03 when the RNA is extended by polymerase. We therefore expect a switch from a high FRET efficiency to a low FRET efficiency once the RNA has been extended *in vitro*.

To confirm that our overhang RNA was active *in vitro* and that our new dye labelling positions did not reduce activity, we performed a fluorescence *in vitro* activity assay. We found that the primer in our replication complex was extended from a 20 mer to a 35 mer upon addition of RdRp WT and ATP alone, whilst addition of RdRp WT and both ATP and UTP resulted in full extension of the primer from a 20 mer to a

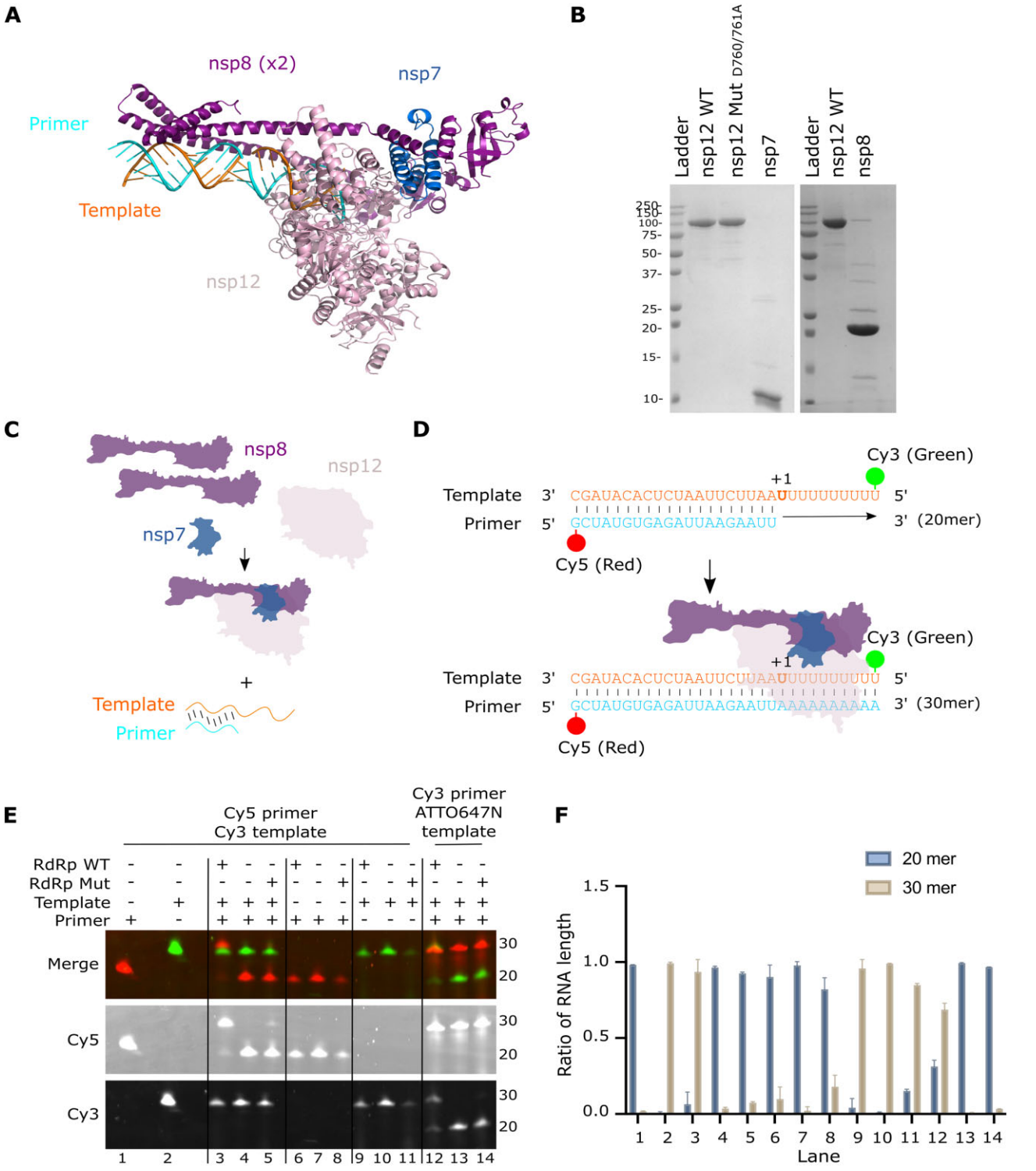

Figure 1. A minimal SARS-CoV-2 RTC is active *in vitro*. (**A**) Cryo-EM structure (PDB: 6YYT) of the SARS-CoV-2 RdRp bound to RNA. A single subunit of nsp12 associates with two copies of nsp8 and one copy of nsp7, which in turn is bound to double-stranded RNA. (**B**) SDS–PAGE gel showing the size and purity of the purified proteins; nsp12 WT, nsp12 active site mutant (D760A/D761A), nsp7, and nsp8. (**C**) Schematic showing assembly of a minimal RTC by preincubation of the three nsps together to form a complex, before incubating with fluorescently labelled pre-annealed template and primer RNAs. (**D**) Sequences of the annealed template (orange) and primer RNA (cyan), before and after RdRp-mediated extension. The template is labelled with Cy3 at position 1 and the primer is labelled with Cy5 at position 30. In the presence of RdRp and NTPs the primer sequence is extended to the same length as the template (30 mer). (**E**) *In vitro* activity assay showing extension of the Cy5 labelled primer from a 20 mer to a 30 mer when RdRp WT, NTPs and both primer and template RNAs are present. (**F**) Quantification of the relative amount of RNA product out of total fluorescence intensity in each lane of the gel based on the position of primer only (20 mer, lane 1) and template only (30 mer, lane 2) controls. Error bars represent standard deviation from two independent repeats.

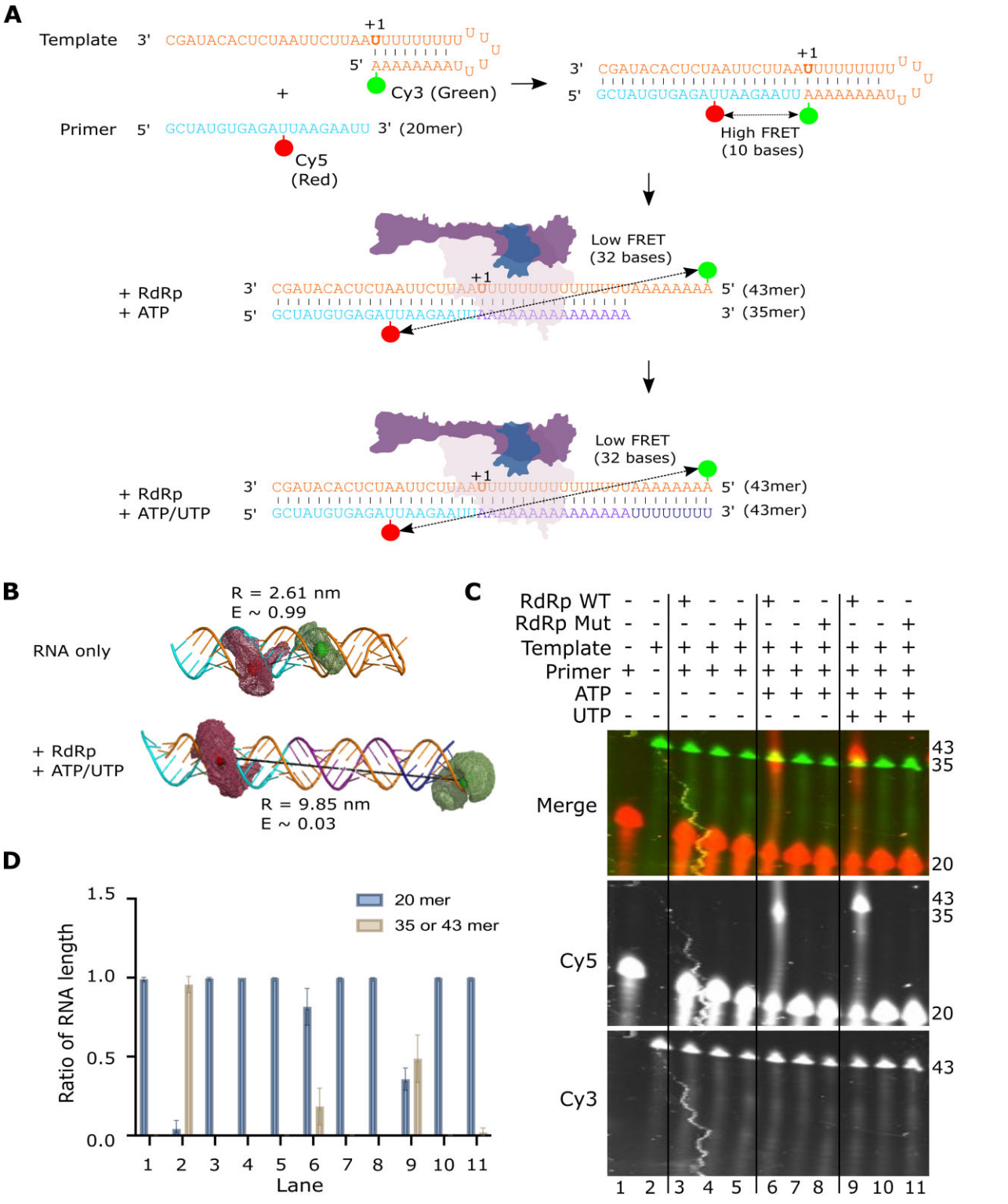

Figure 2. Design of a single-molecule extension assay to detect conformational changes in RNA during replication. (**A**) Schematic showing the design of a single-molecule extension assay. A 43-nucleotide extension RNA template designed to form a self-annealed hairpin labelled with a Cy3 dye at the 5′ end was annealed to a short 20-nucleotide primer sequence, labelled with a Cy5 dye at position 12 (high FRET signature). Upon RdRp and nucleotide addition the primer sequence is extended, separating the two dyes (low FRET signature). (**B**) AV modelling of the fluorescent dyes for nonextended and fully extended RNA. For nonextended RNA the dyes are 2.61 nm apart, giving an estimated FRET, E of 0.99, whilst the extended RNA dyes are an estimated 9.85 nm apart, giving an E ~0.03. (**C**) *In vitro* activity assay showing extension of the Cy5 labelled primer from a 20 mer to a 35 mer or 43 mer when RdRp and ATP or ATP/UTP were added. (**D**) Quantification of the relative products at the 20 mer position and 35 or 43 mer position in each column.

43 mer (Fig. 2C). We quantified this as a ratio of RNA extension from 20 mer to either a 35 mer or 43 mer using the intensity of each band over the total intensity (Fig. 2D), which confirmed that the dsRNA construct can be extended in a nucleotide-dependent manner in the presence of WT polymerase.

Next, we used our overhang RNA construct to measure *in vitro* RdRp-extension using a diffusion-based smFRET assay (Fig. 3 and Supplementary Fig. S1A–E). We incubated the RNA with RdRp and nucleotides before diluting them to picomolar concentrations and measuring smFRET on replication complexes diffusing through the confocal volume. We found that annealed RNA alone produced a high FRET population centred at E = 0.90, confirming that the RNA forms the overhang RNA structure expected from our design (Fig. 3A). As a control, we annealed a double-stranded RNA that mimics the expected product predicted from full extension of the primer and found that, as expected, this produced a significantly lower FRET population with mean E = 0.19 (Fig 3B). Addition of RdRp and ATP only resulted in two distinct FRET populations, a high FRET population representing nonextended overhang RNA (E = 0.90) and a low FRET population which represents partially extended RNA (E = 0.22) (Fig. 3C). Addition of RdRp and both ATP and UTP results in full extension of the RNA primer, resulting in a major FRET population centred at E = 0.18, representing fully extended RNA, and a minor population of nonextended overhang RNA (E = 0.90) (Fig. 3D). The assay using both ATP and UTP with the active site mutant nsp12 (D760A/D761A) showed no extension of the RNA, resulting in a major RNA population centred at E = 0.90 (Fig. 3E).

We also confirmed that we were able to get similar results with different dye labelling positions and different primer and template sequences. We showed that moving the Cy5 dye from position 12 to position 19 on the primer abrogated extension activity (Supplementary Fig. S2A–C), possibly because the dye prevented RdRp binding or was too close to the active site, however extension was observed when the position of the Cy3 dye on the template was changed from position 1 to position 3 (Supplementary Fig. S2D–F). Furthermore, a longer RNA duplex that can make contact with the N-terminal poles of nsp8, as shown in the structure by Hillen *et al.* (2020) [12] was also assessed using the smFRET assay. Similarly to the shorter RNA constructs, the longer RNA only also produced a high FRET population representing nonextended overhang RNA E = 0.83) that could be extended to a low FRET RNA population centered at E = 0.03 upon addition of RdRp and NTPs (Supplementary Fig. S2G–I). We also ran the assay with other control conditions, including where the RNA was unable to self-anneal to form the overhang by replacing the poly-A sequence in the template with a poly-C sequence and showed the FRET efficiency remained low in the RNA only condition (E = 0.31), indicative of a linear RNA structure (Supplementary Fig. S2J). The wider FRET distribution in this control also suggests that when the hairpin is not formed the template is free to move around widely. Finally, we assessed a construct where the primer RNA included a poly(A) extension to mimic the partially extended state (Supplementary Fig. S2K). We found that this population was centred at a lower value than the sample where the RNA was partially extended by the RdRp (E = 0.13 compared to E = 0.22 in Fig. 3C); possibly because in experimental conditions the RdRp is present and may be stalled on the RNA, holding it in a less flexible conformation and thus resulting in a higher FRET efficiency.

Interestingly, we observed that addition of ATP only also resulted in a lower conversion of overhang RNA to extended RNA compared to addition of both ATP and UTP (Supplementary Fig. S1F). As described above, we hypothesized that addition of ATP only may lead to stalling of the RdRp on the partially extended replication complexes, therefore leaving fewer RdRp molecules available to replicate the RNA in the sample. In contrast, addition of both ATP and UTP should result in run-off of the RdRp from the end of the extended RNA, resulting in a readily available RdRp population that can further replicate any free RNAs in the sample. We confirmed our hypothesis by analysing the replication complexes on a native gel, which allowed us to see the complexes formed. The double-stranded RNA control that mimics the expected product predicted from full extension of the primer provided a marker for the expected size of the fully extended RNA complex (Supplementary Fig. S3, lane 2), whilst addition of RdRp resulted in a larger complex that represents polymerase-bound RNA (Supplementary Fig. S3, lane 3). As expected, addition of RdRp and ATP only led to increased stabilization of the RdRp–RNA complex (Supplementary Fig. S3, lane 4), whilst addition of RdRp with ATP and UTP resulted in a similar amount of complex to lane 3 (Supplementary Fig. S3, lane 5), confirming that run-off of the RdRp occurs when the RNA is fully extended. Overall, our results indicate that the movements of RNA that occur during SARS-CoV-2 RdRp-mediated RNA extension can be efficiently captured by single-molecule FRET assays, and that these results are consistent with *in vitro* activity assay observations.

Single-molecule FRET shows inhibition of RdRp by remdesivir

Having shown that our assay was able to capture RdRp-mediated RNA extension at the single-molecule level, we next sought to investigate the molecular mechanisms of replication inhibition. Remdesivir triphosphate is a licensed adenosine triphosphate analogue shown previously to inhibit SARS-CoV-2 RdRp. The proposed mechanism for remdesivir inhibition of RdRp is by delayed chain termination, whereby remdesivir triphosphate binds in place of ATP to hydrogen bond with UTP, and three more NTPs are added to the nascent strain before steric hinderance prevents further translocation and induces RdRp stalling (Fig. 4A). We used a denaturing gel to show RdRp extension of a primer RNA in the presence of increasing concentrations of remdesivir with either high NTP (500 μM final ATP/UTP) or low NTP (5 μM final ATP/UTP) concentrations. Surprisingly, in high NTP conditions, we observed an increase in the fully extended 43 mer product with increasing remdesivir concentration, suggesting that ATP and UTP are still being incorporated and that remdesivir itself may be mis-incorporated into the growing product (Fig. 4B). We do observe some chain termination with 5 mM remdesivir, although a strong band representing the full-length product is also present. In low NTP conditions, significantly less full extension is observed and in the 5 mM remdesivir condition only partially extended primer products are produced (Fig. 4B).

Having established that remdesivir has an inhibitory effect on RdRp extension of our overhang RNA, we went on to image complexes using confocal smFRET. As expected from our denaturing gel results, we observed that in high NTP

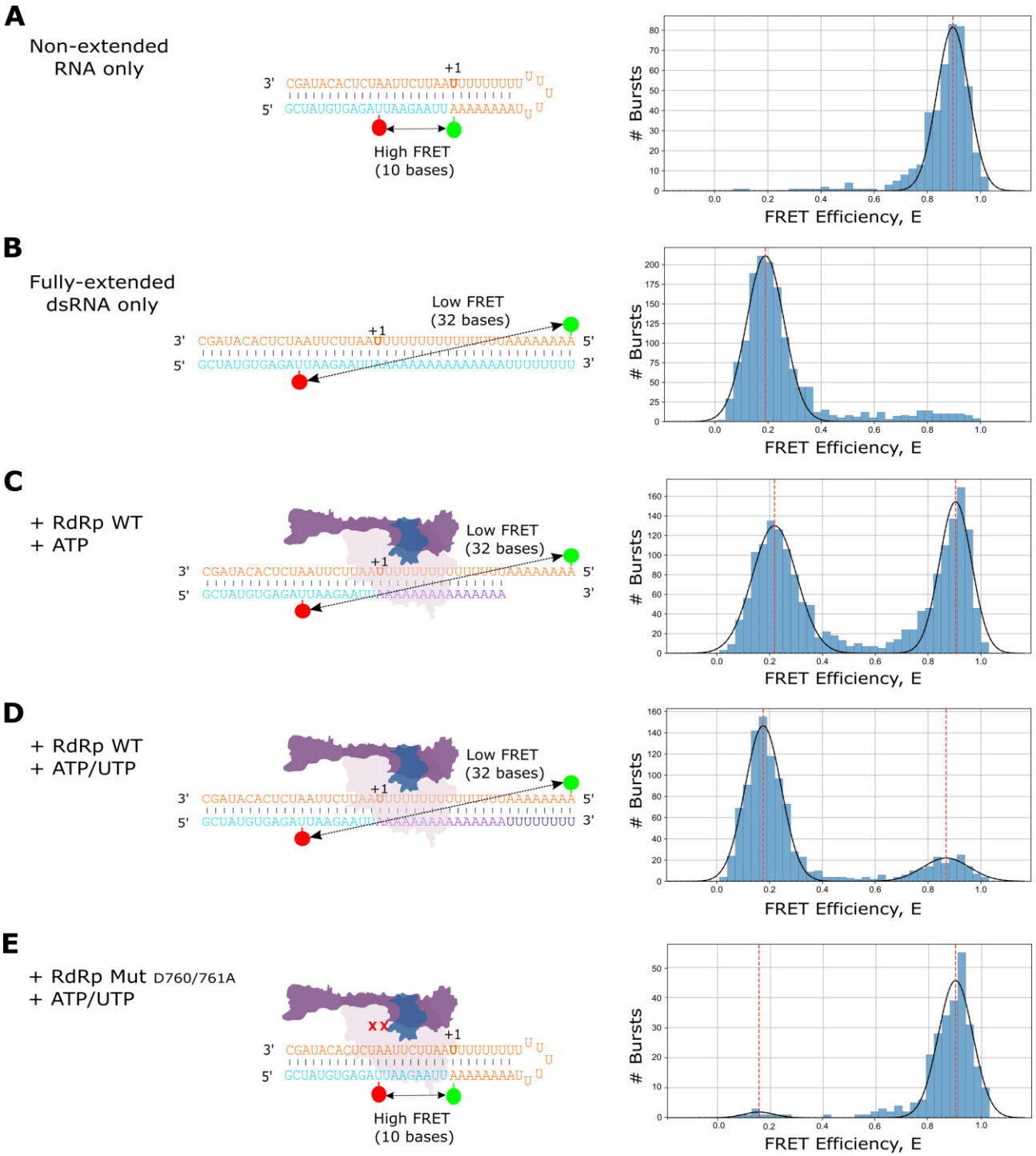

Figure 3. Single-molecule FRET can be used to measure RNA extension by the SARS-CoV-2 RdRp. (**A**) FRET efficiency (E) when a Cy3-labelled 43 mer template and Cy5-labelled 20 mer primer were annealed without RdRp. (**B**) A double-stranded RNA control that mimics the expected product predicted from full extension of the primer gives an expected low FRET population. (**C**) Addition of RdRp and ATP to the pre-annealed RNA results in two distinct FRET populations (nonextended and partially extended RNA). (**D**) Addition of RdRp and ATP/UTP extends the 20 mer primer to a 43 mer, resulting in almost complete RNA extension. (**E**) Same as panel (D), except using the RdRp mutant with nsp12 D760A/D761A (represented by XX in the figure).

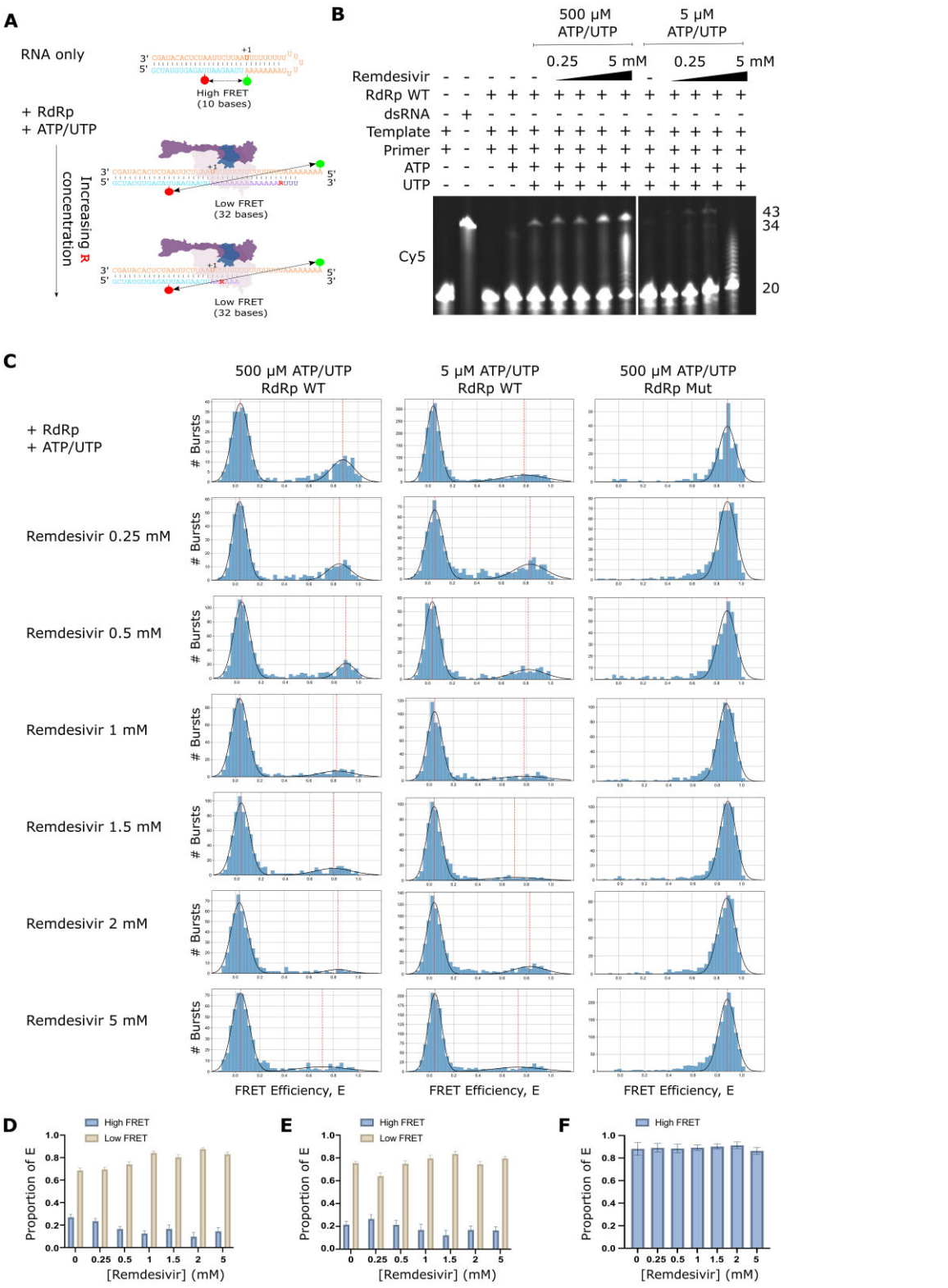

Figure 4. Inhibition of RNA extension with remdesivir. (**A**) Schematic of the proposed delayed chain termination mechanism of action of the ATP analogue remdesivir (denoted by 'R'). (**B**) Denaturing gel showing RdRp extension of a Cy5-labelled primer in the presence of ATP and UTP in increasing concentrations of remdesivir with either a high NTP (500 μM final) or low NTP (5 μM final) concentration. (**C**) FRET efficiencies, E, for RNA conformations during extension by the RdRp in high NTP (500 μM final) concentration conditions or low NTP conditions (5 μM final), with either WT or mutant D670/671A RdRp. (**D**–**F**) Quantification of the high and low FRET populations in panel (C) as a proportion of the total FRET distributions by finding the probability density function. Error bars represent standard error of the Gaussian fit.

conditions, increasing concentrations of remdesivir resulted in an increase in the low FRET population representative of extended RNA, and a corresponding decrease in the high FRET population representative of nonextended overhang RNA (Fig. 4C and D). Unexpectedly, however, we observed a similar pattern in smFRET assays of the low NTP concentration conditions (Fig. 4C and E), which contrasts from our gel results which suggested that we should observe a greater population of nonextended overhang compared to extended RNA. Exchange of the WT RdRp for the D760A/D761A mutant confirmed that extension was reliant on having an active RdRp present (Fig. 4C and F).

RdRp stalling plays a role in remdesivir inhibition

To further investigate our low NTP concentration smFRET results, we used a 4%–15% gradient native gel to observe RdRp–RNA complexes with increasing concentrations of remdesivir, in both high (500 μM) and low (5 μM) NTP concentrations (Fig. 5A and B). We incubated RdRp with RNA and 500 μM ATP/UTP and observed a strong band corresponding to the fully extended double-stranded RNA product on the gel resulting from run-off of the RdRp from the RNA, as well as a minor shifted band representing RNA that remained bound by the RdRp (Fig. 5B, lane 1). Addition of remdesivir resulted in large complexes representing partially extended, RdRp-bound, RNA products (Fig. 5B, lanes 2–5). Increasing concentrations of remdesivir resulted in an increasingly shifted band, suggesting that the RdRp was increasingly stalled on the increasingly extended RNA as remdesivir was incorporated. In low NTP conditions (5 μM ATP/UTP), no visible fully extended RNA product was observed (Fig. 5B, lane 6), demonstrating that NTPs were limiting and full-length extension was inhibited. We expected that limiting NTP conditions would force remdesivir incorporation and chain termination, and consistent with this expectation, found that even low concentrations of remdesivir resulted in significant RdRp stalling on the RNA (Fig. 5B, lanes 7–10). These results suggest that the extent of RdRp stalling on the viral RNA is heavily dependent on the concentration of natural NTPs.

To further investigate the role of RdRp stalling in SARS-CoV-2 replication inhibition by remdesivir we used FCS, a method that measures the fluorescence intensity fluctuations of diffusing complexes, providing information on their diffusion rates using temporal autocorrelation. Rhodamine 6G was used as a standard to quantify the confocal volume parameters before RNA only or RNA-protein complexes were measured in either high (500 μM; Fig. 5C) or low (5 μM; Fig. 5D) NTP concentrations, and normalized correlations were plotted against lag time. At 500 μM ATP and UTP concentrations we observed a shift to longer lag times in all cases where RdRp was present compared to RNA only, as expected from the slower diffusion of larger complexes (Fig. 5C). The addition of remdesivir, however, did not result in an additional increase in the diffusion time of the RNA in nonlimiting natural NTP conditions (Fig. 5C). In comparison, when remdesivir was added to the reaction with a final concentration of just 5 μM ATP and UTP, the diffusion time increased compared to similar conditions without remdesivir present (Fig. 5D), supporting our other observations that there is increased stalling of the RdRp on the RNA when remdesivir is incorporated in low NTP conditions. We therefore conclude that in low NTP conditions remdesivir acts to inhibit the SARS-CoV-2 RdRp by delayed chain termination brought about by stalling the RdRp on the viral RNA, whilst in high NTP conditions the RNA can still be fully extended; the mechanism of action of remdesivir is therefore not only dependent on inhibitor concentration but also on the concentration of competing NTPs.

We repeated our experiments without NTPs altogether in a native gel, which showed that RdRp cannot extend overhang RNA to produce fully dsRNA without NTPs, and when remdesivir only was added in increasing concentrations a bound RdRp–RNA complex was observed (Supplementary Fig. 4A). Furthermore, a Cy5-labelled 20 mer primer was fully extended to a 43 mer product in the presence of the RdRp and remdesivir but no NTPs (Supplementary Fig. 4B), suggesting that remdesivir molecules were incorporated into the product in the absence of NTPs. Our smFRET assay also corroborated these results, showing that the hairpin RNA was extended and resulting in low FRET populations when RdRp and remdesivir only were added (Supplementary Fig. 4C and D). Together, this suggests that remdesivir can be incorporated in the nascent RNA.

Single-molecule FRET shows inhibition of RdRp by a non-nucleoside analogue inhibitor

To test inhibition of the SARS-CoV-2 RdRp by a non-nucleoside analogue inhibitor we assessed the impact of suramin addition to our assay. Suramin is a broad-spectrum inhibitor of viruses and parasites and has been shown to inhibit SARS-CoV-2 infection in cell culture by preventing cellular entry of the virus [38] as well as inhibiting the viral polymerase by binding at two sites on the protein and blocking the binding of the RNA template strand and preventing entry of product RNA into the active site [22] (Fig. 6A). A denaturing gel where increasing concentrations of suramin were added to the reactions showed that extension of the overhang RNA was inhibited in a concentration-dependent manner (Fig. 6B), which was supported by a native gel showing that fully extended RNA decreases in a similar way (Fig. 6C). These results were supported by our single-molecule FRET experiments, in which increasing concentrations of suramin resulted in a decrease in the low FRET population representative of extended RNA (Fig. 6D). Quantification of the ratios of low FRET and high FRET distributions supported this finding (Fig. 6E). In summary, we have shown that single-molecule FRET can be a useful method to assess inhibition of the SARS-CoV-2 RdRp by a non-nucleoside inhibitor.

Discussion

Despite the devastating impact of the COVID-19 pandemic, many of the molecular details of coronavirus replication remain unknown. Here, we have expressed and purified the minimal protein components of the SARS-CoV-2 replication complex and shown that these are capable of actively extending RNA labelled with fluorophores. Although this complex has previously been shown to extend radiolabelled RNA [13], we have developed fluorescence-based extension assays to test RdRp activity without the need for radioactive components. This novel approach has allowed us to study SARS-CoV-2 minimal replication complexes using fluorescence-based *in vitro* activity assays and single-molecule imaging. To measure RdRp-mediated replication using smFRET, we used a unique ‘overhang’ RNA template that was designed to form

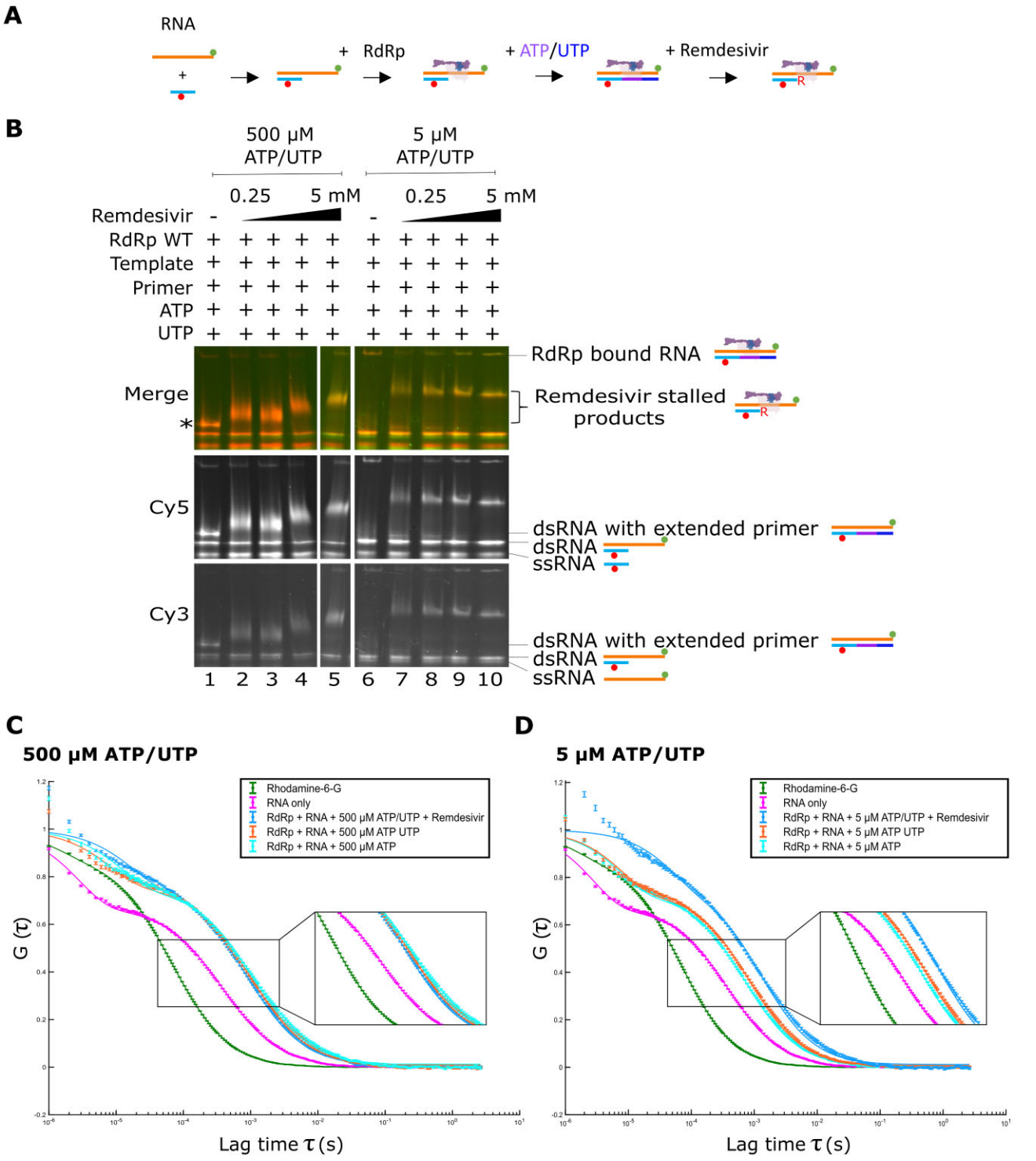

Figure 5. RdRp stalls on RNA in low NTP conditions. (**A**) Schematic of RdRp binding to the fluorescently labelled RNA during NTP and remdesivir addition. (**B**) Native gel showing remdesivir-enabled RdRp stalling on RNA in the presence of either 500 μM or 5 μM final NTP concentrations. * denotes the position of the extended double stranded RNA. (**C**) FCS comparing the diffusion of RNA only with RdRp-bound RNA in the presence of a 500 μM final concentration of nucleotides and remdesivir. Rhodamine 6G was used as a calibration reference. (**D**) FCS comparing the diffusion of RNA only with RdRp-bound RNA in the presence of a 5 μM final concentration of nucleotides and remdesivir.

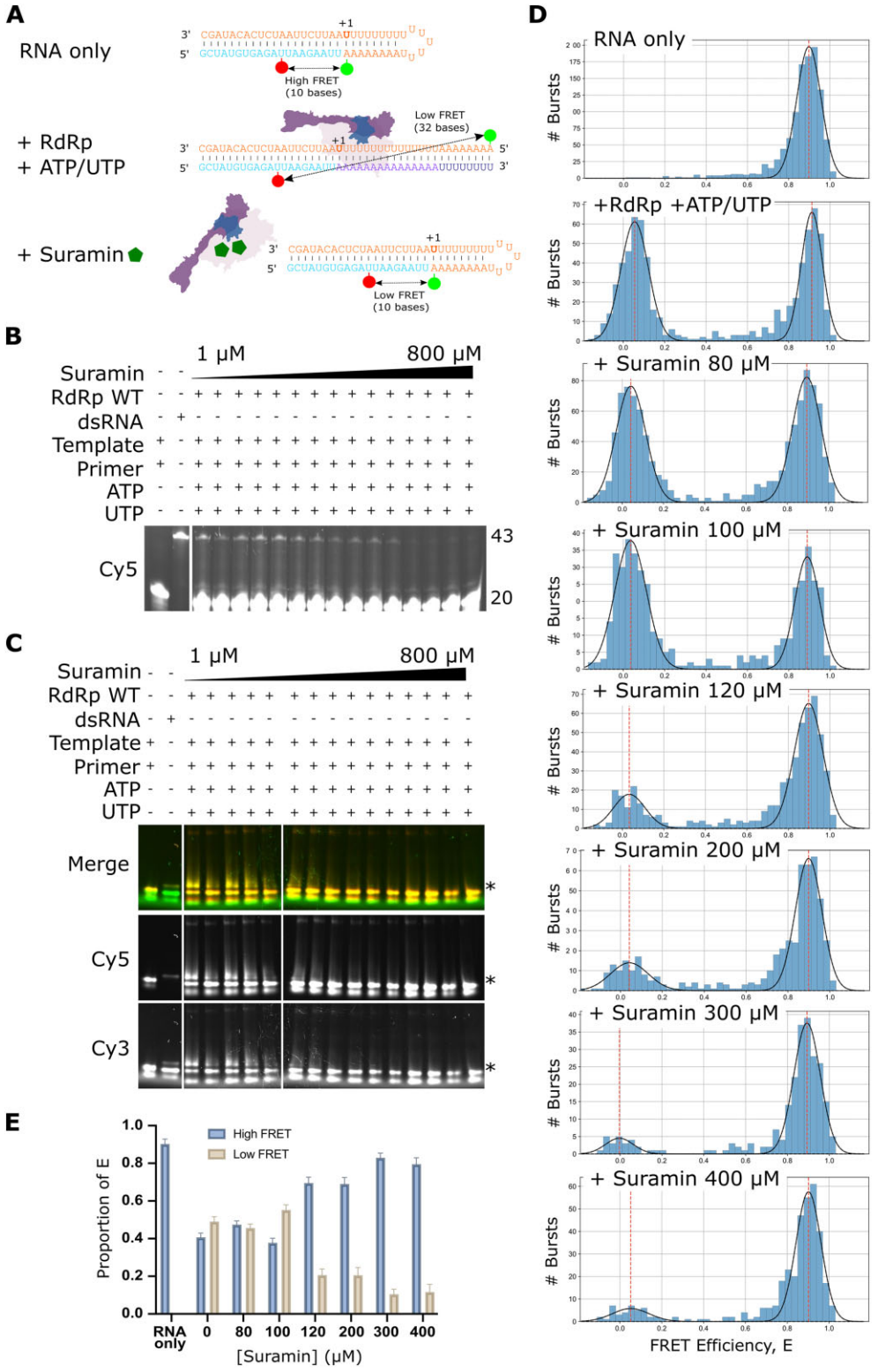

Figure 6. Single-molecule FRET analysis of RdRp inhibition by the non-nucleoside inhibitor suramin. (**A**) Schematic of the proposed mechanism of action of suramin. The binding of two suramin molecules blocks the binding of the RdRp to the RNA template–primer duplex as well as the entry of NTPs into the catalytic site. (**B**) Denaturing gel showing inhibition of RdRp extension of a Cy5-labelled primer in the presence of ATP and UTP in increasing concentrations of suramin. (**C**) Native gel showing inhibition of fully extended primer product in increasing concentrations of suramin. * denotes the position of the extended double stranded RNA. (**D**) FRET efficiencies, E, for RNA conformations during extension by the RdRp in increasing concentrations of suramin. (**E**) Quantification of the high and low FRET populations in panel (C) as a proportion of the total FRET distributions. Error bars represent standard deviation of the Gaussian fit.

a self-annealed hairpin that upon nucleotide addition to the primer strand would open and cause a decrease in the expected FRET signature. We were also able to control nucleotide addition through the template design, ensuring that either partial or full RNA extension took place. Our assays allowed us to observe SARS-CoV-2 RdRp-mediated extension of RNA at the single-molecule level, and to assess the impact of both non-nucleoside and nucleoside analogue inhibitors on extension.

Remdesivir is a direct-acting antiviral agent that is used to treat patients with severe COVID-19 disease by targeting the viral RdRp of SARS–CoV-2. Despite having broad-spectrum antiviral activity against a wide variety of viruses, the mechanisms of action of remdesivir are not fully understood. The triphosphate form of remdesivir competes with its natural counterpart ATP for incorporation into viral RNA, thought to lead to delayed chain termination [19, 20]. Our gels and single-molecule FRET experiments showed, however, an increase in the fully extended RNA product with increasing remdesivir concentration when the natural ATP and UTP were at a high concentration of 500 μM. This is in agreement with a previous observation that RNA synthesis arrest can be overcome with higher concentrations of natural nucleotide pools [20]. Interestingly, intracellular NTP concentrations are in the high μM and low mM range [39], which suggests that in the presence of remdesivir, continued RNA synthesis is likely to occur under biologically relevant conditions. If continued RNA synthesis occurs in a cellular context it is likely that remdesivir itself may be mis-incorporated into the growing product, a hypothesis supported by our data. It has therefore been suggested that the primer strand, and by extension the negative-sense copy of the viral genome, could contain several remdesivir residues [21]. Inefficient incorporation of UTP opposite remdesivir molecules in the genome may therefore provide a second explanation for how remdesivir inhibits SARS-CoV-2 replication [21], by template-dependent inhibition.

In contrast to remdesivir inhibition in high NTP conditions, our gels showed that significantly less full extension was observed when natural ATP and UTP were at a lower concentration of 5 μM. This result was not reflected in our single-molecule FRET experiments, however, which showed a similar pattern to that observed in high NTP concentration conditions, where a greater population of fully extended RNA was observed than nonextended overhang RNA. This was explained by using native gel electrophoresis and FCS to show that in limiting natural NTP conditions increasing concentrations of remdesivir resulted in increasingly more protein stalling on the RNA. Stalled RdRp would be expected to sit on the RNA template and hold it in an extended conformation, thus resulting in a low FRET signature. Our results are consistent with other findings, for instance, studies that provided a structural analysis of RdRp stalling by remdesivir [40, 41] and showed that RdRp translocation is prevented by the sterically impaired passage of the cyano group in remdesivir past the serine-861 side chain in the nsp12 subunit of RdRp. A second study that used a single-molecule magnetic-tweezers platform also showed that the barrier induced by the clash of remdesivir with serine-861 was sufficiently strong to elicit polymerase stalling and backtracking [42]. Taken together, this suggests that the predominant mechanism of remdesivir action against the SARS-CoV-2 RdRp may be dependent on the surrounding concentration of competing NTPs.

Our fluorescence-based single-molecule FRET assays also proved to be a useful technique to assess inhibition of the SARS-CoV-2 RdRp by suramin, a non-nucleoside inhibitor. Suramin was first described over one hundred years ago, and has been shown to be effective at inhibiting the replication of a wide range of viruses, including enteroviruses, Zika virus, Chikungunya, Ebola, and SARS-CoV-2 [43]. A cryo-EM structure of suramin bound to the SARS-CoV-2 RdRp revealed that suramin bound to the RdRp active site, blocking the binding of both RNA template and primer strands [22]. This mechanism of action was supported by our single-molecule FRET results, which showed that increasing concentrations of suramin resulted in a decrease in extended RNA.

The minimal RTC used in our experiments does not incorporate other important viral nsps involved in replication, such as the multifunctional nsp14 enzyme which has 3′–5′ exoribonuclease and methyltransferase activity [44], or the helicase nsp13 [45]. Nevertheless, our findings are consistent with several other studies of SARS-CoV-2 viral replication and our simple system has the potential for additional nsps to be added to allow us to mechanistically study their function at the single-molecule level.

In summary, our results advance our understanding of the interactions of the SARS-CoV-2 RdRp with RNA and a variety of viral inhibitors. As the RdRp complexes of SARS-CoV, MERS-CoV, and SARS–CoV-2 have all been suggested to be inhibited by remdesivir via a delayed chain termination mechanism it is likely that all three of these dangerous viruses exhibit common mechanisms of inhibition; our results therefore provide the potential to study alternative mechanisms of action for other viral RdRps and inhibitors. Our unique single-molecule hairpin RNA design therefore not only offers a useful way to rapidly screen multiple compounds for potential antiviral activity, but also offers the ability to disentangle the exact mechanisms of inhibition of inhibitor compounds, all of which is crucial to allow us to screen for and design new generations of antivirals.

Acknowledgements

Author contributions: D.G. and N.C.R. conceptualized the study and wrote the manuscript. D.G., R.C., A.M., H.F., J.S., and A.D performed experiments. D.G. and R.C. analysed and visualized the data. J.R.K. E.F., and N.C.R. contributed with project administration, supervision, resources, and funding acquisition. All authors commented on the manuscript and approved the submitted version.

Supplementary data

Supplementary data is available at NAR online.

Conflict of interest

None declared.

Funding

This work was supported by a Royal Society Dorothy Hodgkin Research Fellowship [DKR00620 and RGF\R1\180054 to N.R.]; and Medical Research Council programme grants [MR/R009945/1 and MR/X008312/1

to E.F.]; and Medical Research Council G2P-UK National Virology consortium grant [MR/W005611/1 to E.F.].

Data availability

The data underlying this article are available in the article and in its online supplementary material.

References

1. Coronaviridae Study Group of the International Committee on Taxonomy of Viruses. The species *severe acute respiratory syndrome-related coronavirus*: classifying 2019-nCoV and naming it SARS-CoV-2. *Nat Microbiol* 2020;**5**:536–44. https://doi.org/10.1038/s41564-020-0695-z
2. Hamre D, Procknow JJ. A new virus isolated from the human respiratory tract. *Exp Biol Med* 1966;**121**:190–3. https://doi.org/10.3181/00379727-121-30734
3. McIntosh K, Dees JH, Becker WB *et al.* Recovery in tracheal organ cultures of novel viruses from patients with respiratory disease. *Proc Natl Acad Sci USA* 1967;**57**:933–40. https://doi.org/10.1073/pnas.57.4.933
4. Van Der Hoek L, Pyrc K, Jebbink MF *et al.* Identification of a new human coronavirus. *Nat Med* 2004;**10**:368–73. https://doi.org/10.1038/nm1024
5. Woo PCY, Lau SKP, Chu C *et al.* Characterization and complete genome sequence of a novel coronavirus, coronavirus HKU1, from patients with pneumonia. *J Virol* 2005;**79**:884–95. https://doi.org/10.1128/JVI.79.2.884-895.2005
6. Masters PS. The molecular biology of coronaviruses. *Adv Virus Res* 2006;**66**:193–292. https://doi.org/10.1016/S0065-3527(06)66005-3
7. Sola I, Mateos-Gomez PA, Almazan F *et al.* RNA-RNA and RNA-protein interactions in coronavirus replication and transcription. *RNA Biology* 2011;**8**:237–48. https://doi.org/10.4161/rna.8.2.14991
8. Sawicki SG, Sawicki DL. A new model for coronavirus transcription. *Adv Exp Med Biol* 1998;**440**:215–9. https://doi.org/10.1007/978-1-4615-5331-1_26
9. Wang Q, Wu J, Wang H *et al.* Structural basis for RNA replication by the SARS-CoV-2 polymerase. *Cell* 2020;**182**:417–28. https://doi.org/10.1016/j.cell.2020.05.034
10. Gao Y, Yan L, Huang Y *et al.* Structure of the RNA-dependent RNA polymerase from COVID-19 virus. *Science* 2020;**368**:779–82. https://doi.org/10.1126/science.abb7498
11. Peng Q, Peng R, Yuan B *et al.* Structural and biochemical characterization of the nsp12-nsp7-nsp8 core polymerase complex from SARS-CoV-2. *Cell Rep* 2020;**31**:e70968. https://doi.org/10.1016/j.celrep.2020.107774
12. Hillen HS, Kokic G, Farnung L *et al.* Structure of replicating SARS-CoV-2 polymerase. *Nature* 2020;**584**:154–6. https://doi.org/10.1038/s41586-020-2368-8
13. Walker AP, Fan H, Keown JR *et al.* The SARS-CoV-2 RNA polymerase is a viral RNA capping enzyme. *Science* 2020;**49**:779–82. https://doi.org/10.1126/science.abb7498
14. Yin W, Mao C, Luan X *et al.* Structural basis for inhibition of the RNA-dependent RNA polymerase from SARS-CoV-2 by remdesivir. *Science* 2020;**368**:1499–504. https://doi.org/10.1126/science.abc1560
15. Tomescu AI, Robb NC, Hengrung N *et al.* Single-molecule FRET reveals a corkscrew RNA structure for the polymerase-bound influenza virus promoter. *Proc Natl Acad Sci USA* 2014;**111**:E3335–42. https://doi.org/10.1073/pnas.1406056111
16. Lam AM, Murakami E, Espiritu C *et al.* PSI-7851, a pronucleotide of β-d-2′-deoxy-2′-fluoro-2′-C-methyluridine monophosphate, is a potent and pan-genotype inhibitor of Hepatitis C Virus replication. *Antimicrob Agents Chemother* 2010;**54**:3187–96. https://doi.org/10.1128/AAC.00399-10
17. Warren TK, Jordan R, Lo MK *et al.* Therapeutic efficacy of the small molecule GS-5734 against Ebola virus in rhesus monkeys. *Nature* 2016;**531**:381–5. https://doi.org/10.1038/nature17180
18. Tchesnokov EP, Feng JY, Porter DP *et al.* Mechanism of inhibition of ebola virus RNA-dependent RNA polymerase by Remdesivir. *Viruses* 2019;**11**:326. https://doi.org/10.3390/v11040326
19. Gordon CJ, Tchesnokov EP, Feng JY *et al.* The antiviral compound remdesivir potently inhibits RNA-dependent RNA polymerase from Middle East respiratory syndrome coronavirus. *J Biol Chem* 2020;**295**:4773–9. https://doi.org/10.1074/jbc.AC120.013056
20. Gordon CJ, Tchesnokov EP, Woolner E *et al.* Remdesivir is a direct-acting antiviral that inhibits RNA-dependent RNA polymerase from severe acute respiratory syndrome coronavirus 2 with high potency. *J Biol Chem* 2020;**295**:6785–97. https://doi.org/10.1074/jbc.RA120.013679
21. Tchesnokov EP, Gordon CJ, Woolner E *et al.* Template-dependent inhibition of coronavirus RNA-dependent RNA polymerase by remdesivir reveals a second mechanism of action. *J Biol Chem* 2020;**295**:16156–65. https://doi.org/10.1074/jbc.AC120.015720
22. Yin W, Luan X, Li Z *et al.* Structural basis for inhibition of the SARS-CoV-2 RNA polymerase by suramin. *Nat Struct Mol Biol* 2021;**28**:319–25. https://doi.org/10.1038/s41594-021-00570-0
23. Yan L, Ge J, Zheng L *et al.* Cryo-EM structure of an extended SARS-CoV-2 replication and transcription complex reveals an intermediate State in cap synthesis. *Cell* 2021;**184**:184–93. https://doi.org/10.1016/j.cell.2020.11.016
24. York A, Hengrung N, Vreede FT *et al.* Isolation and characterization of the positive-sense replicative intermediate of a negative-strand RNA virus. *Proc Natl Acad Sci USA* 2013;**110**:E4238–45. https://doi.org/10.1073/pnas.1315068110
25. Bieniossek C, Richmond TJ, Berger I. MultiBac: multigene baculovirus-based eukaryotic protein complex production. *Curr Protoc Protein Sci* 2008;**Chapter 5**:Unit 5.20. https://doi.org/10.1002/0471140864.ps0520s51
26. Antczak M, Popenda M, Zok T *et al.* New functionality of RNAComposer: application to shape the axis of miR160 precursor structure. *Acta Biochim Pol* 2016;**63**:737–44. https://doi.org/10.18388/abp.2016_1329
27. Popenda M, Szachniuk M, Antczak M *et al.* Automated 3D structure composition for large RNAs. *Nucleic Acids Res* 2012;**40**:e112. https://doi.org/10.1093/nar/gks339
28. Kalinin S, Peulen T, Sindbert S *et al.* A toolkit and benchmark study for FRET-restrained high-precision structural modeling. *Nat Methods* 2012;**9**:1218–25. https://doi.org/10.1038/nmeth.2222
29. Förster T. Zwischenmolekulare Energiewanderung und Fluoreszenz. *Ann Phys* 1948;**437**:55–75. https://doi.org/10.1002/andp.19484370105
30. Clegg RM. Fluorescence resonance energy transfer and nucleic acids. *Methods Enzymol* 1992;**211**:353–88. https://doi.org/10.1016/0076-6879(92)11020-j
31. Buckhout-White S, Spillmann CM, Algar WR *et al.* Assembling programmable FRET-based photonic networks using designer DNA scaffolds. *Nat Commun* 2014;**5**:5615. https://doi.org/10.1038/ncomms6615
32. Kapanidis AN, Lee NK, Laurence TA *et al.* Fluorescence-aided molecule sorting: analysis of structure and interactions by alternating-laser excitation of single molecules. *Proc Natl Acad Sci USA* 2004;**101**:8936–41. https://doi.org/10.1073/pnas.0401690101
33. Ingargiola A, Lerner E, Chung SY *et al.* FRETBursts: an open source toolkit for analysis of freely-diffusing single-molecule FRET. *PLoS One* 2016;**11**:160716. https://doi.org/10.1371/journal.pone.0160716
34. Schrimpf W, Barth A, Hendrix J *et al.* PAM: a framework for Integrated analysis of imaging, single-molecule, and ensemble fluorescence data. *Biophys J* 2018;**114**:1518–28. https://doi.org/10.1016/j.bpj.2018.02.035

35. Culbertson CT, Jacobson SC, Michael Ramsey J. Diffusion coefficient measurements in microfluidic devices. *Talanta* 2002;**56**:365–73. https://doi.org/10.1016/s0039-9140(01)00602-6
36. Nir E, Michalet X, Hamadani KM *et al.* Shot-noise limited single-molecule FRET histograms: comparison between theory and experiments. *J Phys Chem B* 2006;**110**:22103–24. https://doi.org/10.1021/jp063483n
37. Subissi L, Posthuma CC, Collet A *et al.* One severe acute respiratory syndrome coronavirus protein complex integrates processive RNA polymerase and exonuclease activities. *Proc Natl Acad Sci USA* 2014;**111**:E3900–9. https://doi.org/10.1073/pnas.1323705111
38. Salgado-Benvindo C, Thaler M, Tas A *et al.* Suramin inhibits SARS-CoV-2 infection in cell culture by interfering with early steps of the replication cycle. *Antimicrob Agents Chemother* 2020;**64**:e00900–20. https://doi.org/10.1128/AAC.00900-20
39. Traut TW. Physiological concentrations of purines and pyrimidines. *Mol Cell Biochem* 1994;**140**:1–22. https://doi.org/10.1007/BF00928361
40. Bravo JPK, Dangerfield TL, Taylor DW *et al.* Remdesivir is a delayed translocation inhibitor of SARS-CoV-2 replication. *Mol Cell* 2021;**81**:1548–52. https://doi.org/10.1016/j.molcel.2021.01.035
41. Kokic G, Hillen HS, Tegunov D *et al.* Mechanism of SARS-CoV-2 polymerase stalling by remdesivir. *Nat Commun* 2021;**12**:279. https://doi.org/10.1038/s41467-020-20542-0
42. Seifert M, Bera SC, Van Nies P *et al.* Inhibition of SARS-CoV-2 polymerase by nucleotide analogs from a single-molecule perspective. *eLife* 2021;**10**:e70968. https://doi.org/10.7554/eLife.70968
43. Wiedemar N, Hauser DA, Mäser P. 100 years of suramin. *Antimicrob Agents Chemother* 2020;**64**:e01168–19. https://doi.org/10.1128/AAC.01168-19
44. Lin S, Chen H, Chen Z *et al.* Crystal structure of SARS-CoV-2 nsp10 bound to nsp14-ExoN domain reveals an exoribonuclease with both structural and functional integrity. *Nucleic Acids Res* 2021;**49**:5382–92. https://doi.org/10.1093/nar/gkab320
45. Chen J, Malone B, Llewellyn E *et al.* Structural basis for helicase-polymerase coupling in the SARS-CoV-2 replication-transcription complex. *Cell* 2020;**182**:1560–73. https://doi.org/10.1016/j.cell.2020.07.033

Received: October 17, 2024. **Revised:** April 8, 2025. **Editorial Decision:** April 12, 2025. **Accepted:** April 16, 2025